# Lowermost mantle flow at the eastern edge of the African Large Low Shear Velocity Province

CrossMark

Heather A. Ford *, Maureen D. Long, Xiaobo He [1], Colton Lynner

*Department of Geology and Geophysics, Yale University, New Haven, CT, USA*

### ABSTRACT

Observations of seismic anisotropy in the lowermost mantle are plentiful, but their interpretation in terms of mantle flow remains challenging. Here we interrogate the anisotropic structure of the lowermost mantle beneath the Afar region, just outside the edge of the African Large Low Shear Velocity Province, using a combination of shear wave splitting techniques applied to phases propagating at five distinct raypath orientations. We then model the resulting data set by testing various candidate mechanisms for anisotropy. The observations are best fit by a model that invokes the lattice preferred orientation (LPO) of post-perovskite, with the [100] crystallographic axis oriented either nearly vertically or highly obliquely to the horizontal plane. Plausible corresponding mantle flow scenarios involve a significant vertical flow component, which suggests that the African Large Low Shear Velocity Province edge may deflect ambient mantle flow upwards or may be associated with a sheet-like upwelling.

© 2015 Elsevier B.V. All rights reserved.

## 1. Introduction

The African Large Low Shear Velocity Province (LLSVP) is a well-established feature of global tomography models and, in combination with the Pacific LLSVP, dominates the seismic structure of the lower mantle (e.g., Lekic et al., 2012). The properties, origin, dynamics, and longevity of LLSVPs are debated (e.g., Davies et al., 2012). Specifically, it is unclear whether LLSVPs are long-lived, stable structures that anchor mantle dynamics (Dziewonski et al., 2010) or whether they represent passive structures aggregated by subduction-driven flow above the CMB (McNamara and Zhong, 2005). The sides of LLSVPs are thought to be seismically sharp and steeply dipping (e.g., Ni et al., 2002; Wang and Wen, 2007; Sun and Miller, 2012), and their margins may represent possible zones of plume generation (Torsvik et al., 2008).

Observations of seismic anisotropy are often used to shed light on dynamic processes in the Earth's mantle. Seismic anisotropy is commonly observed in the upper mantle, while the bulk of the lower mantle is generally thought to be isotropic (Meade et al., 1995). The D″ layer at the base of the mantle is an exception (e.g., Kendall and Silver, 1996; Panning and Romanowicz, 2006); observations of anisotropy in the lowermost mantle are abundant (Nowacki et al., 2011), but their relationship to mantle dynamics remains unclear. There is debate over whether D″ anisotropy is the result of lattice-preferred orientation (LPO) of one or more mineral phases or the shape-preferred orientation (SPO) of elastically distinct material such as partial melt (Karato, 1998; Nowacki et al., 2011). Uncertainty also exists over the mineralogical composition of the lowermost mantle (which may vary laterally; e.g., Cobden et al., 2012) and whether the dominant mineral phase is $MgSiO_3$ perovskite (bridgmanite) or its high-pressure post-perovskite (ppv) polymorph.

Most body wave studies of D″ anisotropy are effectively limited to a single set of (usually horizontal) raypaths, due to the uneven distribution of sources and receivers at the Earth's surface, with a few exceptions (Wookey and Kendall, 2008; Nowacki et al., 2010). When regions of D″ are sampled from a single orientation, it hampers our ability to distinguish among the different possible mechanisms for lowermost mantle anisotropy, as the anisotropic geometry is not tightly constrained. Here, we overcome this common observational limitation by interrogating a single region of D″ just outside the edge of the African LLSVP (Fig. 1) using a combination of splitting techniques applied to rays propagating at five distinct orientations. This observational strategy allows us to constrain the anisotropic geometry more tightly than possible with a single propagation direction. The methods and results of our shear wave splitting analysis are described in Section 2. We then implement a set of mineral-physics based forward models that test a variety of elastic tensors and orientations that correspond to a range of potential mantle flow scenarios, as discussed in Section 3.
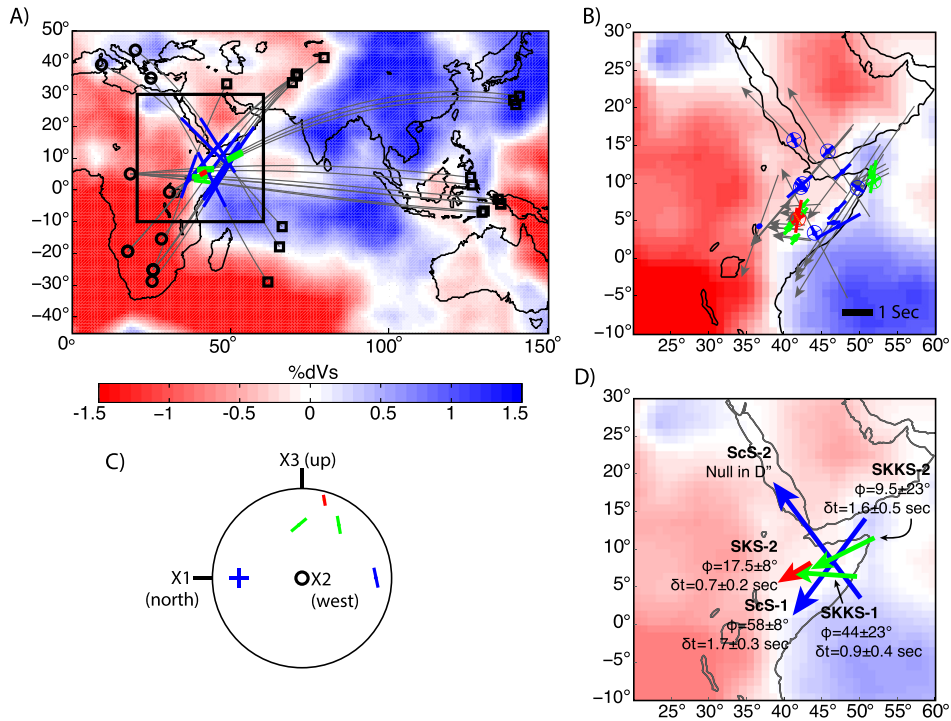
* Corresponding author at: Department of Geology and Geophysics, Yale University, PO Box 208109, New Haven, CT 06520-8109, USA.
*E-mail address:* heather.ford@yale.edu (H.A. Ford).
[1] Now at: Ocean College, Zhejiang University, Hangzhou, China.

**Fig. 1.** (A) Raypaths used in this study (gray lines), with event (squares) and station (circles) locations. Thick solid lines indicate portions of the raypaths sampling D″ for ScS (blue), SKKS (green) and SKS (yellow). Background colors indicate S velocity anomalies at 2650–2900 km depth from the GyPSuM tomography model (Simmons et al., 2010). (B) Individual splitting measurements for ScS (blue), SKKS (green) and SKS (yellow), plotted at the midpoint of the D″ portion of the raypath (gray arrows). Orientation and length of the bars correspond to $\phi$ (clockwise from north) and $\delta t$ (in seconds), respectively, as measured at the station. Circles with cross-hairs indicate null arrivals, with initial polarization direction (thick line). (C) Spherical projection of raypath-averaged $\phi$, using the same plotting convention as in later figures. (D) Schematic of raypath-averaged splitting parameters. Arrows correspond to the average raypaths of ScS (blue), SKKS (green) and SKS (yellow) through D″. SKS and SKKS path lengths are exaggerated (2×) for clarity. Groups ScS-1, ScS-2, SKKS-1 and SK(K)S-2 are referred to in Tables 1 and 2. (For interpretation of the references to color in this figure legend, the reader is referred to the web version of this article.)

This allows us to discriminate which mechanisms and orientations are compatible with the observations. Finally, the range of permissible models is interpreted in terms of plausible mantle flow scenarios at the edge of the African LLSVP (Section 4).

## 2. Shear wave splitting: methods and results

### 2.1. Station selection and measurement methods

We present measurements for SKS, SKKS, and ScS phases recorded at stations in Africa and Europe that sample a region just outside the African LLSVP beneath the Afar region (Fig. 1). Our study region was carefully selected such that the raypaths sample a region of D″ just outside the LLSVP edge, with little or no sampling of structure within the LLSVP itself. Just to the south of our study area, the location of the LLSVP edge has been well constrained via waveform modeling techniques (Wang and Wen, 2004), but directly beneath Afar the best constraints on the location of the structure's edge come from tomographic models. In particular, the cluster analysis of Lekic et al. (2012) demonstrates that the LLSVP boundary here is relatively well constrained, although there is some uncertainty given the imperfect resolution of global tomographic models.

We measure splitting over a range of raypath propagation directions using differential S–ScS (Wookey et al., 2005a, 2005b; Wookey and Kendall, 2008; Nowacki et al., 2010) and discrepant SKS–SKKS splitting (Niu and Perez, 2004; Long, 2009; He and Long, 2011; Lynner and Long, 2014). Each of these methods relies on a thorough characterization of upper mantle anisotropy beneath the seismic station so that the effects of receiver-side anisotropy can be properly accounted for. In this study, we restricted our analysis to stations which met two criteria, following Lynner and

Long (2013): 1) good backazimuthal coverage for SK(K)S phases that was sufficient to evaluate the presence of complex anisotropy (multiple anisotropic layers, dipping symmetry axes) beneath the receiver, and 2) SK(K)S splitting patterns that reflect either a lack of splitting at the frequencies examined in this study, or simple splitting that indicates the presence of a single horizontal layer of anisotropy beneath the station.

A total of 9 stations were selected for use in this study: BGCA, BOSA, DIVS, IDI, LBTB, LSZ, MBAR, TSUM, and VSL. SK(K)S splitting patterns for several of these stations at the frequencies of interest were documented previously by Lynner and Long (2014), while stations DIVS and VSL were newly evaluated for this study. One station used here (MBAR) has been previously categorized as "complex" for the purpose of characterizing source-side anisotropy beneath subduction zones (Lynner and Long, 2013). However, MBAR exhibits null SKS arrivals over a large swath of backazimuths, including all four backazimuthal quadrants, and only a few non-null SK(K)S measurements, most of which are associated with discrepant SKS–SKKS pairs. For the purpose of this study, therefore, we have characterized MBAR as a "null" station with little or no splitting associated with upper mantle anisotropy beneath the receiver; we attribute the complex (discrepant) SKS–SKKS splitting to D″ anisotropy in our study region. Station locations and associated upper mantle anisotropy corrections can be found in Tables 1 and 2.

Differential S–ScS splitting measurements were carried out using the method of Wookey et al. (2005a, 2005b). Briefly, this method uses the difference in splitting between direct S waves (which do not sample the D″ layer) and ScS waves (which propagate nearly horizontally through D″) to isolate the contribution to splitting from the lowermost mantle. We selected events of magnitude Mw ≥ 5.5 at epicentral distances between 60° and 85° for

**Table 1**
ScS measurements from our study, along with station and event information. For each measurement, the associated source-side and station-side splitting parameters are listed ($\phi$, $\delta t$), as measured at the station, along with the D″-associated splitting of the ScS phase (last two columns). The initial polarization direction (IPD) was measured directly from the waveform for all null ScS arrivals (that is, those that were not split by D″ anisotropy) using the technique of Vidale (1986).

| | Station | | | Event | | | Source side | | Station side | | IPD | ScS (in D″) | |
|---|---|---|---|---|---|---|---|---|---|---|---|---|---|
| | Sta | Sta lat | Sta lon | Evt lat | Evt lon | Depth | Phi | $\delta t$ | Phi | $\delta t$ | Phi | Phi | $\delta t$ |
| ScS-1 | BOSA | −28.6 | 25.3 | 36.3 | 70.9 | 141 | NA | null | NA | null | NA | **61 ± 8** | **3.3 ± 0.3** |
| | TSUM | −19.2 | 17.6 | 36.1 | 70.7 | 129 | 32 ± 8 | 0.8 ± 0.2 | NA | null | NA | **49 ± 6** | **2.2 ± 0.4** |
| | LBTB | −25.0 | 25.6 | 33.5 | 48.8 | 7 | 159 ± 5 | 0.65 ± 0.2 | NA | null | NA | **63 ± 9** | **0.4 ± 0.2** |
| | LBTB | −25.0 | 25.6 | 33.9 | 69.5 | 10 | 165 ± 12 | 0.4 ± 0.2 | NA | null | NA | **83 ± 11** | **0.9 ± 0.3** |
| | LSZ | −15.3 | 28.2 | 36.5 | 71.0 | 185 | 120 ± 15 | 1.6 ± 0.3 | NA | null | NA | **47 ± 6** | **1.5 ± 0.2** |
| | LBTB | −25.0 | 25.6 | 36.4 | 70.8 | 220 | 105 ± 10 | 0.4 ± 0.2 | NA | null | NA | **45 ± 7** | **1.7 ± 0.3** |
| | TSUM | −19.2 | 17.6 | 36.0 | 70.7 | 107 | NA | null | NA | null | −51/129 | **NA** | **null** |
| | TSUM | −19.2 | 17.6 | 36.5 | 71.0 | 187 | NA | null | NA | null | −38/142 | **NA** | **null** |
| | LBTB | −25.0 | 25.6 | 41.7 | 79.4 | 22 | 167 ± 10 | 1.52 ± 0.3 | NA | null | −55/125 | **NA** | **null** |
| ScS-2 | VSL | 39.5 | 9.4 | −11.4 | 66.3 | 10 | NA | null | 79 ± 8 | 1.9 ± 0.3 | −24/156 | **NA** | **null** |
| | IDI | 35.3 | 24.9 | −28.8 | 61.7 | 7 | −63.3 ± 16 | 0.9 ± 0.3 | −5 ± 24 | 1 ± 0.45 | −28/152 | **NA** | **null** |
| | DIVS | 44.1 | 20.0 | −17.8 | 65.4 | 6 | NA | null | 110 ± 10 | 1.77 ± 0.3 | 43/223 | **NA** | **null** |

**Table 2**
SKS and SKKS measurements from our study, along with station and event information. Station-side fast directions ($\phi$) and delay times ($\delta t$) correspond to the splitting due to upper mantle anisotropy beneath the station, which is removed in our analysis. The final four columns report the splitting parameters for SKS and SKKS phases that can be attributed to D″ anisotropy.

| | Station | | | Event | | | Station side | | SKS (in D″) | | SKKS (in D″) | |
|---|---|---|---|---|---|---|---|---|---|---|---|---|
| | Sta | Sta lat | Sta lon | Evt lat | Evt lon | Depth | Phi | $\delta t$ | Phi | $\delta t$ | Phi | $\delta t$ |
| SKKS-1 | BGCA | 5.2 | 18.4 | −6.9 | 129.2 | 150 | NA | null | NA | null | **37.5 ± 23** | **0.9 ± 0.5** |
| | BGCA | 5.2 | 18.4 | −6.5 | 129.9 | 148 | NA | null | NA | null | **60.9 ± 29** | **0.7 ± 0.4** |
| | BGCA | 5.2 | 18.4 | −4.3 | 135.1 | 33 | NA | null | NA | null | **42.2 ± 31** | **0.9 ± 0.6** |
| | BGCA | 5.2 | 18.4 | −4.2 | 135.1 | 33 | NA | null | NA | null | **38 ± 24** | **1 ± 0.5** |
| | BGCA | 5.2 | 18.4 | −2.8 | 134.3 | 33 | NA | null | NA | null | **46.6 ± 21** | **1 ± 0.3** |
| | BGCA | 5.2 | 18.4 | 1.7 | 126.1 | 103 | NA | null | NA | null | **40.5 ± 18** | **0.8 ± 0.2** |
| | BGCA | 5.2 | 18.4 | 4.1 | 125.6 | 150 | NA | null | NA | null | **42 ± 15** | **1.1 ± 0.3** |
| SK(K)S-2 | MBAR | −0.6 | 30.7 | 29.6 | 141.0 | 98 | NA | null | NA | null | **9 ± 26** | **0.9 ± 0.3** |
| | MBAR | −0.6 | 30.7 | 28.4 | 139.2 | 486 | NA | null | **30 ± 6** | **0.75 ± 0.2** | **10 ± 20** | **2.2 ± 0.8** |
| | MBAR | −0.6 | 30.7 | 27.0 | 139.9 | 527 | NA | null | **5 ± 10** | **0.65 ± 0.2** | **NA** | **null** |

analysis. A bandpass filter that retained energy at periods between 8 and 50 s was applied to all waveforms. Following Wookey et al. (2005a, 2005b), direct S phases were first corrected for the effect of anisotropy beneath the receiver ($\Gamma_R$, estimated from SKS phases) and their splitting was then measured to obtain splitting parameters for anisotropy in the upper mantle near the source ($\Gamma_S$). The splitting operators in the source ($\Gamma_S$) and receiver ($\Gamma_R$) regions were then used to measure splitting in the D″ region ($\Gamma_{D''}$) from the ScS waveform. The measurement method applies a grid search over a range of possible $\phi$ and $\delta t$ values for $\Gamma_{D''}$; for each pair of potential splitting parameters attributable to D″ anisotropy, the effects of $\Gamma_R$, $\Gamma_{D''}$, and $\Gamma_S$ are removed from the waveform in order by sequentially rotating and time-shifting the horizontal components. The pair of $\phi$ and $\delta t$ values that most nearly linearizes the corrected particle motion of the ScS phase, as measured by the covariance between the horizontal components, corresponds to the D″-associated splitting. An example of a differential S–ScS splitting measurement is shown in Fig. 2.

SKS–SKKS splitting measurements were carried out following Long (2009). In general, SKS and SKKS splitting measurements for the same event-station pair typically agree, as demonstrated by global studies (e.g., Niu and Perez, 2004). For the minority of cases in which they do not agree, significant discrepancies are typically attributed to anisotropy in the lowermost mantle (Long, 2009), although finite frequency effects may also make a small contribution to observed discrepancies (Lin et al., 2014). We selected events of magnitude Mw ≥ 5.8 at epicentral distances between 108° and 122° for analysis; as for the ScS/S phases, a bandpass filter that retained energy at periods between 8 and 50 s was applied to all waveforms. We measured SKS and SKKS splitting parameters at

stations BGCA and MBAR by simultaneously applying the rotation-correlation and transverse component minimization measurement methods (as implemented in the SplitLab software of Wüstefeld et al., 2008) and identified several SKS–SKKS pairs that exhibited clearly discrepant splitting (that is, the $2\sigma$ error bars for each individual measurement do not overlap; see Long, 2009).

### 2.2. Shear wave splitting results

We obtained a total of high-quality measurements for 12 ScS phases, 8 SKKS phases, and 2 SKS phases that sample the region of interest. Our strict station selection criteria and measurement quality control procedures mean that our dataset is relatively small, but the measurements are well constrained and consistent within each raypath group. Our ScS-S analysis yielded 12 sets of splitting parameters for ScS anisotropy in D″ (Table 1), including 6 null and 6 non-null measurements. For ScS, the group of measurements propagating to the southwest exhibits an average $\delta t$ of $1.7 \pm 0.3$ s, and an average $\phi$ of $58 \pm 8°$. In contrast, the group of three ScS arrivals propagating to the northwest exhibits no discernable splitting (Fig. 1).

Our SKS–SKKS analysis at station BGCA reveals that the SKS observations are consistently null and sample the D″ region within the interior of the African LLSVP, in agreement with other observations from the region (Lynner and Long, 2014). Since these raypaths do not intersect our region of interest, we do not consider them further. The corresponding SKKS splits, which do sample the region of interest (Fig. 1), average $\phi = 44 \pm 23°$ and $\delta t = 0.9 \pm 0.4$ s. For station MBAR, both SKS ($\phi = 17.5 \pm 8°$; $\delta t = 0.7 \pm 0.2$ s) and SKKS ($\phi = 9.5 \pm 23°$; $\delta t = 1.55 \pm 0.5$ s) phases sample the re-
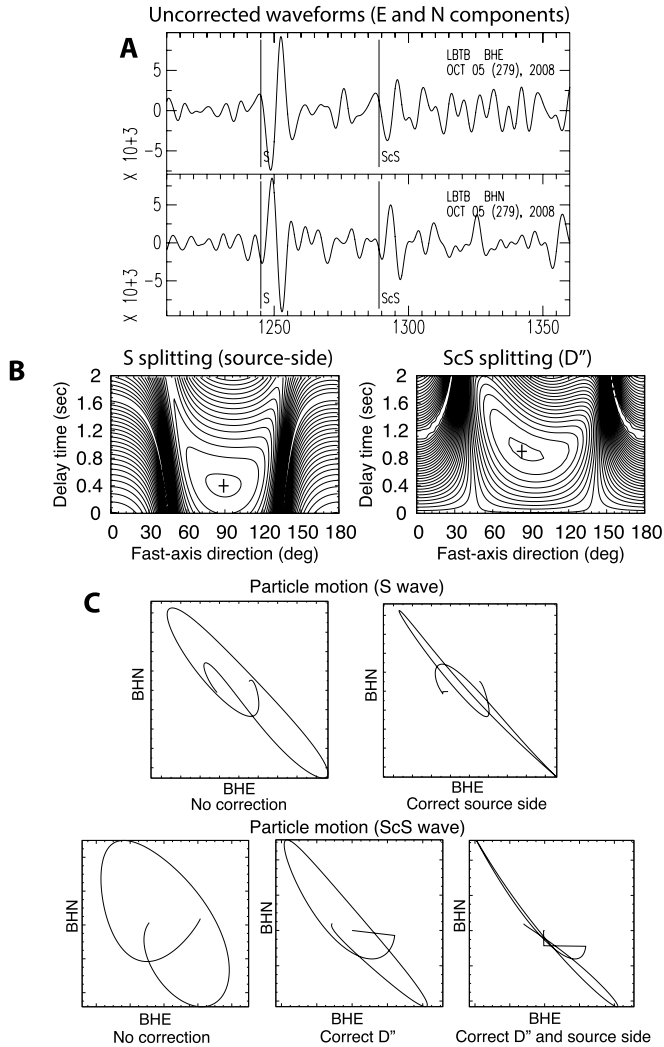
**Fig. 2.** Example of a non-null ScS measurement that reflects a contribution to splitting from D″ anisotropy, measured at station LBTB. (A) Uncorrected horizontal component waveforms, with the expected arrival times for the direct S and ScS phases marked. (B) Error spaces for the splitting measurement on the direct S phase (left), which reflects splitting near the earthquake source, and the splitting measurement on the ScS phase (right), which has been corrected for the effect of near-source splitting and which reflects anisotropy in the lowermost mantle. The crosses represent the best-fitting splitting parameters, while the closest contour represents the 95% confidence region. Additional contours represent progressively larger confidence regions, in 5% increments. (C) Particle motion diagrams for the uncorrected S wave (top left) and the S wave corrected for near-source anisotropy (top right), along with the particle motion diagrams for the uncorrected ScS wave (bottom left), the ScS wave corrected for the effect of D″ anisotropy (bottom middle), and the ScS wave corrected for both D″ anisotropy and anisotropy near the source (bottom right).

gion of interest, and both exhibit splitting that is inconsistent with the inferred upper mantle anisotropy signal, as discussed above. We therefore attribute these observations to D″ anisotropy in our study region.

Overall, we measured splitting due to D″ anisotropy for ScS phases from two distinct propagation azimuths ∼100° apart, along with SKS measurements from a single propagation azimuth and SKKS measurements from two propagation azimuths ∼30° apart (Fig. 1). ScS phases propagate nearly horizontally through D″ at the epicentral distance ranges used here, while SK(K)S phases propagate at angles ∼35°–60° from the horizontal. We therefore effectively sample a single region of D″ over five distinct propagation directions. In general, each group of raypaths exhibits coherent splitting behavior (Fig. 1B), with significant splitting identified for 4 of the 5 raypaths.

## 3. Mineral physics-based forward modeling: methods and results

### 3.1. Forward modeling method

To constrain the geometry and mechanism of D″ anisotropy, we carried out ray theoretical forward modeling to identify anisotropy scenarios that are consistent with our observations. We assumed that the anisotropic structure is laterally homogeneous throughout our study area (see Section 4.1 for a more detailed discussion of this assumption) and considered a range of possible mechanisms. Because of the uncertainty in the dominant slip systems and LPO geometry for deformed lower mantle aggregates, we focused on testing single-crystal elastic constants for various minerals, assuming that the anisotropic geometry of a deformed lower mantle rock will resemble the single-crystal geometry, although its strength will likely be considerably lower. Specifically, we tested single-crystal elastic tensors for MgO (Karki et al., 1999), perovskite (Wookey et al., 2005a, 2005b), and ppv (Stackhouse et al., 2005; Wentzcovitch et al., 2006) for a range of lower mantle temperatures. We also considered elastic constants for partial melt SPO (Nowacki et al., 2011), and hexagonally averaged tensors for perovskite and ppv. In all, 12 sets of single-crystal elastic constants were used to model our observations (Table 3).

To carry out the forward modeling, we calculated (simple, nonweighted) average splitting parameters for each of the five raypath groups (2 for ScS, 2 for SKKS, and 1 for SKS). Importantly, we assume that all five raypath groups travel through a region of D″ that is laterally homogeneous (see further discussion in Section 4.1). Splitting parameters were measured in a geographic reference frame at the station, but for the modeling were transformed via a ray-centered coordinate system, following Nowacki et al. (2010). For each group of raypaths, we calculated a simplified (ray-theoretical) average propagation path through D″ using a straight-line raypath assumption. For each group of raypaths, we calculated the average backazimuth and propagation angle from the horizontal and used these values in the forward modeling. For SK(K)S phases, we used the ak135 earth reference model (Kennett et al., 1995) to calculate an average incidence angle for each raypath group. For ScS, we followed the approach of Nowacki et al. (2010) and others and made the simplifying assumption that ScS phases propagate horizontally through D″. This is a (commonly made) simplification; ScS phases may propagate at angles of up to ∼15° from the horizontal at the epicentral distances relevant for our study, but it allows us to treat ScS propagation more simply in the modeling.

We tested all possible orientations for each of the 12 sets of elastic tensors. For each candidate anisotropic model orientation, we carried out a ray theoretical prediction of the splitting parameters ($\phi$, $\delta t$) for each raypath orientation in the splitting dataset. We used the MSAT toolkit (Walker and Wookey, 2012) to solve the Christoffel equation for each propagation path and compared the predictions to observations. Comparisons between predictions and observations (averaged for each raypath group) were done by computing a misfit calculated from the difference in both $\phi$ and (relative) $\delta t$ for each propagation direction to evaluate goodness of fit. Misfit values were computed using a residual sum of squares (RSS), where $n$ equals the number of observations, $y$ is $i$th observation, and $f(x)$ is the corresponding $i$th predicted observation:

$$RSS = \sum_{i=1}^{n} \big(y_i - f(x_i)\big)^2$$

The observations and predictions, for the case described above, include both the polarization direction and the relative delay times. The polarization direction and relative delay time misfits were equally weighted when computing the residual sum of squares, as

**Table 3**
Single-crystal elastic constants used in forward modeling. Notes beneath table reference original source and/or the inputs used in computing the coefficients.

| Phase | P (GPa) | T (K) | C11 (GPa) | C22 | C33 | C12 | C13 | C23 | C44 | C55 | C66 | Density (kg/m³) |
|---|---|---|---|---|---|---|---|---|---|---|---|---|
| ppv[1] | 136 | 3000 | 1198 | 909 | 1183 | 400 | 347 | 500 | 273 | 230 | 360 | 5336 |
| ppv[1] | 135 | 4000 | 1107 | 847 | 1131 | 429 | 318 | 441 | 251 | 221 | 361 | 5262 |
| ppv[2] | 125 | 2500 | 1146 | 888 | 1139 | 454 | 418 | 507 | 311 | 238 | 352 | 5369 |
| ppv[2] | 140 | 4000 | 1119 | 900 | 1131 | 498 | 486 | 536 | 343 | 231 | 326 | 5329 |
| perovskite[2] | 125 | 2500 | 874 | 1095 | 1077 | 539 | 436 | 469 | 311 | 255 | 296 | 5324 |
| perovskite[3] | 126 | 2800 | 808 | 1055 | 993 | 522 | 401 | 472 | 328 | 263 | 262 | 5191 |
| perovskite[3] | 136 | 4000 | 857 | 1130 | 941 | 523 | 383 | 513 | 281 | 263 | 284 | 5194 |
| MgO[4] | 135 | 3000 | 1239 | 1239 | 1239 | 299 | 299 | 299 | 202 | 202 | 202 | 5035 |
| hex ppv[*A] | 135 | 4000 | 1029 | 847 | 1029 | 435 | 408 | 435 | 306 | 311 | 306 | 5262 |
| hex pv[*B] | 136 | 4000 | 902 | 1130 | 902 | 518 | 381 | 518 | 283 | 261 | 283 | 5194 |
| oblate melt[*C] | NA | NA | 1020 | 1026 | 1026 | 443 | 443 | 444 | 291 | 251 | 251 | 5324 |
| tubule melt[*D] | NA | NA | 1026 | 1023 | 1023 | 445 | 445 | 445 | 289 | 290 | 290 | 5324 |

[1] From Stackhouse et al. (2005).
[2] From Wentzcovitch et al. (2006).
[3] From Wookey et al. (2005a, 2005b).
[4] From Karki et al. (1999).
[*A] Calculated using ppv elastic coefficients of Stackhouse et al. (2005) at $T = 4000$ K and averaging method of Montagner and Anderson (1989).
[*B] Calculated using perovskite elastic coefficients of Wookey et al. (2005a, 2005b) at $T = 4000$ K and averaging method of Montagner and Anderson (1989).
[*C] Inputs used to calculate elastic constants. $Vp_{matrix} = 13.9$ km/s; $Vs_{matrix} = 7.9$ km/s; $rho_{matrix} = 5324$ kg/m³; $Vp_{inclusion} = 7$ km/s; $Vs_{inclusion} = 0$ km/s; aspect ratio = 0.01; vol. fraction melt = 0.003. Calculated using MS_effective_medium.m MSAT (Walker and Wookey, 2012) script.
[*D] Inputs used to calculate elastic constants. $Vp_{matrix} = 13.9$ km/s; $Vs_{matrix} = 7.9$ km/s; $rho_{matrix} = 5324$ kg/m³; $Vp_{inclusion} = 7$ km/s; $Vs_{inclusion} = 0$ km/s; aspect ratio = 100; vol. fraction melt = 0.003. Calculated using MS_effective_medium.m MSAT (Walker and Wookey, 2012) script.

described below. For the polarization directions, each of the residuals were normalized by the maximum residual, 90°, before being summed.

Observed delay times are a function of the path length within the anisotropic layer traversed by the shear wave and the strength of the anisotropy, which is itself a function of the single-crystal elastic constants and the strength of LPO. In evaluating delay time misfit, our approach avoids making any explicit assumptions about anisotropy strength. Because of the tradeoff between the strength of anisotropy and the thickness of the anisotropic layer, we chose to compare the relative delay times (RDT) among the averaged raypaths. For both the observed and predicted delay times, the relative difference between two raypaths M and N is the absolute difference divided by the their arithmetic mean:

$$RDT_{obs} = \frac{\delta t_{obsM} - \delta t_{obsN}}{(\delta t_{obsM} + \delta t_{obsN})/2} * 100\%$$

$$RDT_{pre} = \frac{\delta t_{preM} - \delta t_{preN}}{(\delta t_{preM} + \delta t_{preN})/2} * 100\%$$

$$RDT_{residual} = RDT_{obs} - RDT_{pre}$$

Where the predicted delay time ($\delta t_{pre}$) for each path is:

$$\delta t_{pre} = T * \left( \frac{1}{vs_{slow}} - \frac{1}{vs_{fast}} \right)$$

and $T$ is equal to the total path length through D″, assuming a 250 km layer and incidence angles calculated assuming the ak135 earth reference model (Kennett et al., 1995). Total path length for the raypath averaged groups are as follows: ScS-1 = 1618 km; ScS-2 = 1710 km; SKKS-1 = 429 km; SK(K)S-2 = 292 and 428 km.

This method of calculating relative, rather than absolute, delay time misfits allows us to make the comparison between the predicted and observed delay times without having to accurately assume the anisotropic layer thickness and strength in the real Earth. Similarly, as long as the observed raypaths travel through a region of laterally homogeneous D″ thickness, the $RDT_{obs}$ will also be unbiased with respect to layer thickness.

An important consideration in our modeling is how to treat the group of null (that is, non-split) ScS measurements for rays propagating to the northwest (Fig. 1). Null arrivals can be attributed to a lack of (or very weak) splitting along the raypath; alternatively,

a null can be produced when the initial polarization of the phase is aligned parallel to the fast or slow direction of the anisotropic medium (e.g., Long and Silver, 2009). Two of the three ScS nulls in our dataset exhibit similar initial polarization directions (measured directly from the waveform using the method of Vidale, 1986), with the third offset from these directions by ∼70°. Because the $2\sigma$ errors on the individual initial polarization estimates are ∼10°, we cannot completely rule out the possibility that the ScS nulls exhibit essentially perpendicular initial polarization directions. Our forward modeling approach therefore considers both potential explanations (weak splitting vs. initial polarization alignment) for our null ScS observations. However, we consider that weak or absent splitting of ScS phases propagating to the northwest through our study area is much more likely than the alternative explanation.

### 3.2. Forward modeling: illustration and a synthetic example

For each candidate elastic tensor, we tested all possible orientations (in 5° increments in rotation space) and applied the following misfit criteria to identify models that provide a satisfactory fit to the data. Anisotropy scenarios that resulted in differences between observed and predicted fast directions greater than 20° for any of the five propagation directions were discarded, since observational uncertainties in our measurements do not exceed this value. We calculated misfit values for all remaining orientations, but only those that fell within the top 10% of fits (or the 10% with smallest misfit) were considered to provide reasonable fits to the data. The reason for this is that the top 10% encompasses a rate of change in misfit that is significantly larger than it is in the top 50% or 75% (Fig. 3). Visual inspection of more generous thresholds (e.g., 20%, 50%) showed that the number of potential orientation clusters (identified via cluster analysis) did not typically increase, and that in many cases, the 20° polarization misfit threshold often proved to be stringent enough of a criteria to prevent inclusion of additional points at the 20% or 50% level. In some cases, the total misfit for a particular model orientation may be relatively low, but the model is discarded because one or more individual raypaths has a polarization misfit greater than 20° (for example, the pancake-shaped melt SPO scenario shown with a light blue line in Fig. 3).

To illustrate our modeling approach, we show in Fig. 4 an example of the best-fitting orientations obtained for a candidate ppv
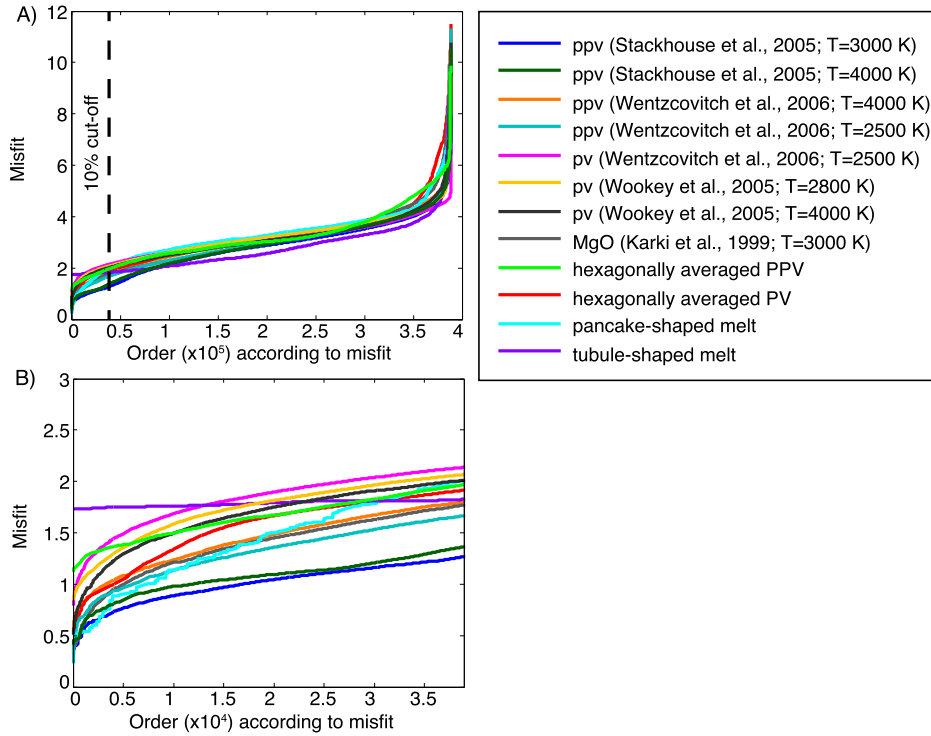
**Fig. 3.** Calculated misfit values (total misfit, including both delay time and directional misfits) for each set of single-crystal elastic constants considered in this study, plotted from the best-fitting model (smallest misfit value) to the worst (largest misfit value). (A) All misfits over all potential orientations. Thick dashed black line indicates top 10% of fits. (B) Top 10% of fits (smallest misfits). It should be noted that (A) and (B) include all possible orientations, including those for which misfits for individual raypaths may not meet the cutoff threshold of less than 20° in fast polarization direction. This explains why the pancake-shaped melt model (light blue line), which has relatively low misfits in certain directions, is discarded as incompatible with the data. (For interpretation of the references to color in this figure legend, the reader is referred to the web version of this article.)

elastic tensor. All permissible orientations that meet our misfit criteria are shown and are color-coded by their overall misfit values (Fig. 4A). For this set of elastic constants, we identified three distinct "clusters" of permissible anisotropy orientations, each of which successfully predicts the observed splitting parameters for all five propagation directions (Fig. 4B).

To demonstrate the ability of our forward modeling method to accurately retrieve the correct orientation of the elastic tensor, we carried out a synthetic modeling example using the elastic tensor of ppv from Stackhouse et al. (2005) calculated at 136 GPa and 3000 K at a random orientation (chosen using a random number generator), as shown in Fig. 5. Utilizing the same averaged incidence angles and azimuths from our study region, we calculated the polarization direction and delay times for each averaged raypath. For the polarization directions, we introduce randomized error ranging from 0 to 15°. Delay times were calculated assuming a 250 km thick D″ layer and normalized by half of the maximum delay time. The resulting synthetic results were then used to forward model the best-fitting orientation. The results of our forward modeling are illustrated in Figs. 5B–C. While our forward modeling approach identifies two orientations that provide satisfactory fits the synthetic data, the best fit matches the actual input orientation (shown in Fig. 5A and the white square in Fig. 5B).

### 3.3. Single-crystal forward modeling results

We carried out forward modeling for all possible orientations of all single-crystal elastic tensors shown in Table 3. This exercise allows us to discard the cases of hexagonally averaged ppv and perovskite, as well as both cases of melt-induced SPO (oblate melt and tubule-shaped melt), as none of these mechanisms produces splitting predictions that are consistent with the observations. While a simple SPO melt mechanism does not match the data, we note that

this does not by itself rule out the presence of partial melt in our study region, or the possibility of melt SPO combined with another mechanism. Because our analysis rules out geometries involving transverse isotropy (hexagonal symmetry), our interpretation represents a significant departure from most previous D″ anisotropy studies, which typically invoke either vertically (VTI) or tilted (TTI) transverse isotropy (Nowacki et al., 2013), although there are exceptions (e.g., Nowacki et al., 2013; Cottaar et al., 2014). For MgO, we identified a limited range of permissible orientations, but only if we allow for the relatively unlikely interpretation of the ScS null measurements (in which they correspond to a fast or slow splitting direction of the medium). Similarly, for perovskite at 4000 K we identified one orientation that provided a satisfactory fit, again relying on the less likely scenario for ScS nulls. For perovskite at 2800 K, no good fits were identified. Therefore, we consider MgO and perovskite to be relatively unlikely mechanisms for D″ anisotropy in our study region, although we cannot completely rule them out.

In contrast to all other mechanisms tested, we were able to identify a number of ppv orientations that robustly fit the data. We tested four sets of elastic constants (Stackhouse et al., 2005; Wentzcovitch et al., 2006) calculated at specific temperatures (2500 K, 3000 K, or 4000 K; Table 3). (We tested elastic constants calculated at temperatures that correspond to reasonable high and low estimates for D″; it would be desirable to test elastic tensors calculated at intermediate temperatures as well, but we were limited to those values found in the literature.) For each candidate elastic tensor, we found orientations that produce good fits to the observations. In several cases, the forward modeling determined several distinct orientations that produce a good fit to the data for a given set of elastic constants, as in the example shown in Fig. 4.
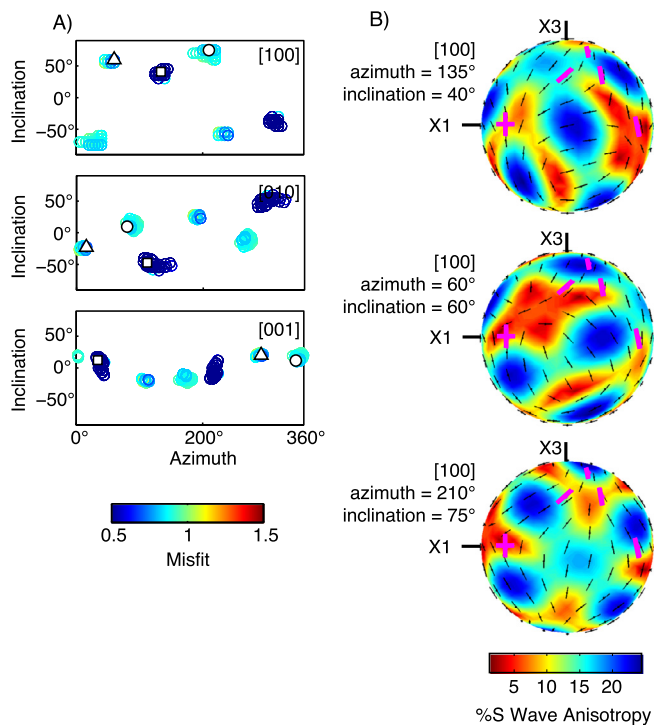
**Fig. 4.** (A) Best-fitting orientations of the [100], [010] and [001] axes of ppv, calculated using elastic constants (4000 K) from Stackhouse et al. (2005). Open circles represent individual orientations; color corresponds to the misfit value. The triangle, square and circle denote the best-fitting orientation of each unique cluster. Other clusters represent redundant (symmetrical) orientations. (B) Shear wave splitting predictions (thin black lines) and observations (magenta lines) for each of the three best-fitting orientations from (A). Each plot represents a spherical projection for all possible wave propagation directions; colors denote predicted anisotropy strength. The magenta cross hairs represent the initial polarization direction (and 90° from the initial polarization direction) for the null ScS observation. In (A) and (B), azimuth refers to the clockwise rotation, in degrees, of the crystallographic axes from North (X1). Inclination refers to the deviation from the horizontal plane (X1–X2), positive up. Note that the view in (B) is shown with X2 (West) oriented out of the page. (For interpretation of the references to color in this figure legend, the reader is referred to the web version of this article.)

In total, we identified 27 combinations of ppv elastic constants and orientations, identified via cluster analysis, which fit our splitting observations. We summarize these results by plotting the orientation of the three crystallographic axes in geographic space (Fig. 6). The permissible models cluster into four robust sets of very similar orientations, which are not affected by the assumptions made in treating the ScS null observations. Interestingly, the positions of these clusters also appear to be independent of the temperature at which the elastic constants were calculated. (There is, however, some dependence on which group of authors calculated the elastic constants. Specifically, Cluster #3 in Fig. 6 is associated only with elastic tensors calculated by Stackhouse et al., 2005, while Cluster #4 is associated only with tensors calculated by Wentzcovitch et al., 2006.) Given the identification of several robust clusters of ppv orientations that provide a good fit to the data, we consider that the LPO of ppv is a likely explanation for the observed shear wave splitting along the eastern edge of the African LLSVP. This is consistent with inferences from several other studies that have attributed D″ anisotropy to the LPO of ppv (Wookey and Kendall, 2008; Nowacki et al., 2010; Cottaar and Romanowicz, 2013).

### 3.4. Forward modeling: polycrystalline aggregates

While the focus of this study is on testing single-crystal elastic constants, we also considered 3 additional sets of elastic con-
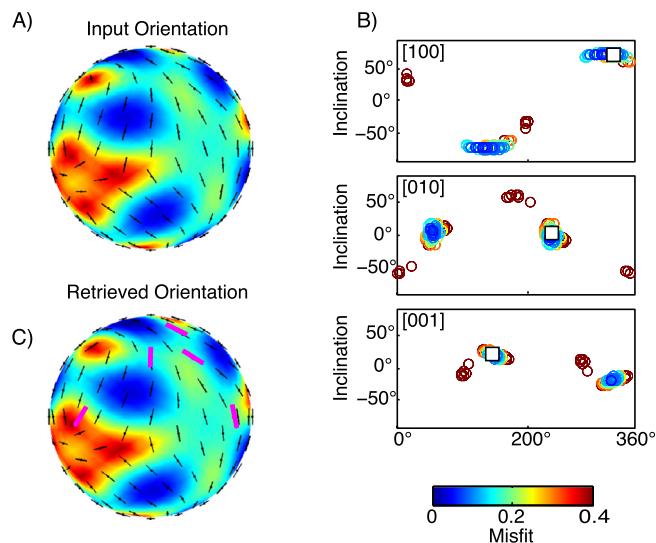


**Fig. 5.** Synthetic forward modeling example. (A) Randomly selected input orientation of ppv (Stackhouse et al., 2005) used to calculate the synthetic observations. (B) Best-fitting orientations of the [100], [010] and [001] axes of ppv retrieved from the synthetic test. Individual, colored, open circles correspond to individual orientations and the color corresponds to the total (delay time and directional) misfit. The white square corresponds to the orientation shown in (A). The large non-marked cluster corresponds to an identical single-crystal orientation (rotated 180°), due to symmetry considerations. (C) Best-fitting orientation determined using the synthetic data from (A) combined with varying amounts of random error. The pink lines show the polarization directions of the synthetic data. (For interpretation of the references to color in this figure legend, the reader is referred to the web version of this article.)

stants produced from a global model of 3D mantle flow and texture development calculated using a visco-plastic self-consistent approach for post-perovskite (Walker et al., 2011). These elastic constants were taken from model TX2008.V1, which corresponds to the lower viscosity model (V1) of Mitrovica and Forte (2004) and the density model (TX2008) from Simmons et al. (2009). We considered 3 sets of constants, corresponding to candidate slip planes (001), (010) and (100). In order to obtain elastic constants that correspond to a simple shear geometry, we selected a point in the model where vertical velocities were close to zero and horizontal velocities were oriented approximately E–W, corresponding to a simple shear geometry with a horizontal shear plane. We then varied the orientation of each set of elastic constants and produced splitting predictions and estimates of misfit, in a manner identical to our single-crystal models.

For the case in which the slip plane was assumed to be (100), we found no orientations that fit the data. In contrast, both (001) and (010) have orientations with acceptable misfits when the ScS null measurements are attributed to weak anisotropy (Fig. 7), and (010) also yielded acceptable orientations when the ScS nulls are considered to be a result of polarization direction alignment (Fig. 7). The misfit values for (010) are significantly lower than for (001), and comparable to our best fits among the 12 single-crystal cases. The implications of the polycrystalline aggregate modeling are discussed further below.

## 4. Discussion

### 4.1. Assumptions regarding laterally homogeneous structure

One of the most fundamental assumptions of our modeling approach is that our observations can be represented using a single uniform geometry of anisotropy that does not vary spatially. This is a significant simplification, but one that is required by our modeling approach. In this study we are testing one possible scenario
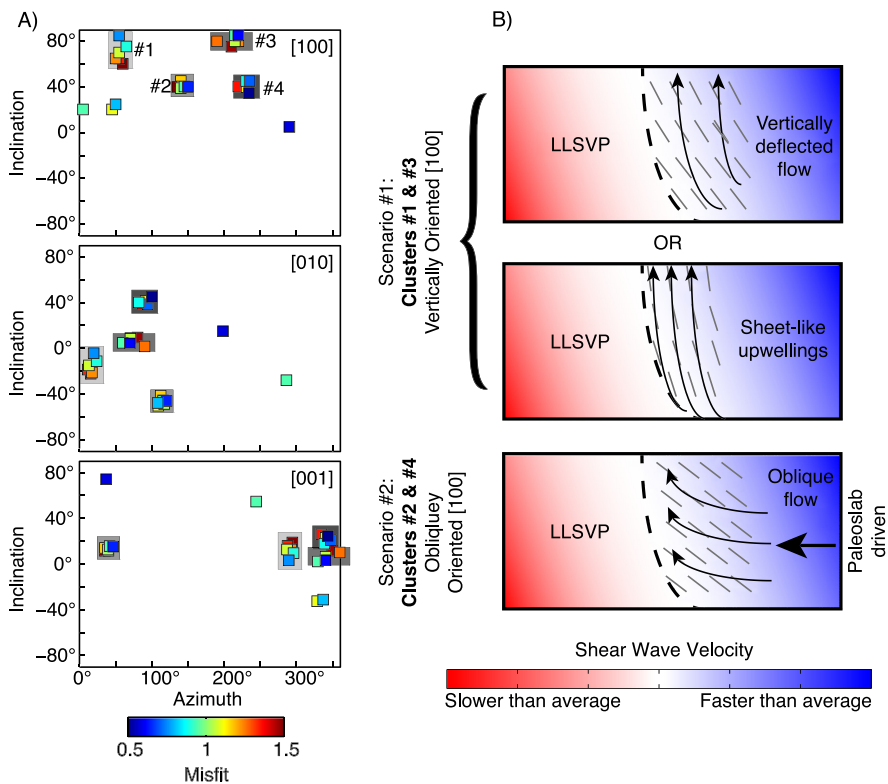
**Fig. 6.** (A) Orientation of the best-fitting [100], [010], [001] crystallographic axes for all 27 single-crystal ppv scenarios consistent with our observations, plotted in geographic space (as in Fig. 4). The color of the individual points corresponds to the misfit value. (B) Schematic cartoon illustrating plausible flow scenarios and maximum finite strain directions (gray sticks) that best fit our forward modeled results. Scenario #1 corresponds to flow with a strong vertical component and a nearly vertical finite strain orientation, inferred from Clusters #1 and #3 in (A). Scenario #2 corresponds to an oblique orientation of finite strain, inferred from Clusters #2 and #4 in (A). (For interpretation of the references to color in this figure legend, the reader is referred to the web version of this article.)
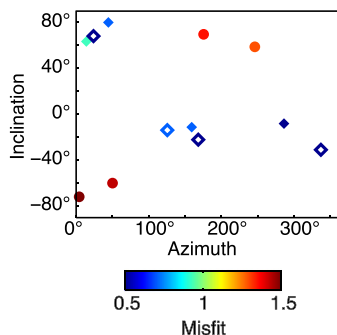


**Fig. 7.** Possible orientations of the shear direction determined through forward modeling of elastic constants produced via texture modeling of polycrystalline ppv aggregates, from Walker et al. (2011). Orientations are plotted in terms of azimuth (degrees from north, x axis) and inclination from the horizontal (degrees, y axis), as in Figs. 4 and 6. Circles correspond to set of elastic constants consistent with deformation along the (001) slip plane, while diamonds correspond to the (010) slip plane. Filled markers indicate that the ScS null was assumed to be due to weak anisotropy in the modeling, open marker correspond to an ScS null produced by alignment of the polarization direction with either the fast or slow axis of symmetry. Colors correspond to the misfit value, as indicated by the colorbar. (For interpretation of the references to color in this figure legend, the reader is referred to the web version of this article.)

(nearly homogeneous anisotropy throughout the study area), but other explanations for our measurements are possible, including small-scale variations in anisotropic structure that are not captured by our modeling approach. Indeed, while we assume generally homogeneous anisotropy in our study region, boundary conditions on mantle flow at the CMB (and perhaps at the LLSVP edge) imply that there must be gradients in anisotropic structure somewhere within the volume of mantle sampled by our measurements. These

gradients are not described by our modeling approach; we assume that these gradients are sharp and localized to the edges of the model volume (for example, just above the CMB), and further assume that our splitting measurements mainly reflect anisotropy within the model volume, away from the edges. Here we discuss how uncertainties in lower mantle mineralogy, thermal structure, and the degree of structural heterogeneity informs our modeling approach, and how our knowledge of the isotropic structure can inform our interpretations.

The lowermost mantle (that is, the core–mantle boundary region) is a thermo-chemical boundary layer, separating the hot, molten, iron outer core from the cooler, silicic, solid mantle. The temperature contrast across the thermal boundary layer is estimated at $1000 \pm 500$ K (Lay et al., 1998) and lateral gradients in thermal structure are also likely to be steep (Burke et al., 2008), with LLSVP temperatures estimated to be at least 200–300 K above ambient mantle temperatures (Garnero, 2000). However, estimates of the absolute temperature at the CMB vary by up to 1000 K ($\sim$3700 to $\sim$4800 K) as well (van der Hilst et al., 2007). Importantly, the phase stabilities of perovskite and post-perovskite depend on temperature, meaning that uncertainties in temperature will be translated into uncertainties in the depth estimate of the boundary between the two phases.

Temperature aside, experimental and ab initio studies offer a range of potential stability scenarios for perovskite and post-perovskite in the lowermost mantle, often based on variations in composition. For example, one set of experiments by Grocholski et al. (2012) found that an MORB-like composition can produce a phase change at $\sim$400 km above the CMB, while a pyrolitic composition would not produce a phase change at mantle depths. Finally, there are large uncertainties in the development of LPO in the lowermost mantle (see Nowacki et al., 2011 for a more detailed

discussion), with significant implications for our interpretation of mantle flow. Given these large uncertainties in the thermal structure, composition, and other properties of the CMB, it is difficult to explicitly model any possible lateral variations in anisotropy due to variations in these properties. Therefore, in this study we implement a simplified treatment that assumes laterally homogeneous anisotropy, although we cannot exclude the possibility of small-scale heterogeneity in anisotropy.

We have compared our raypath distribution (Fig. 1) to the cluster analysis of Lekic et al. (2012), which uses a number of tomographic models to identify the likely boundary of the African LLSVP, to ensure that our measurements reflect anisotropy just outside the LLSVP and are not sampling the border itself. Based on the cluster analysis, the most likely location of the LLSVP border lies to the west of all our measurements, with the possible exception of the westernmost ScS path (Fig. 1). We are therefore confident that our measurements and modeling reflect anisotropy outside the LLSVP border, if the border is in fact accurately constrained from tomographic imaging. This is an important point, as several studies have argued for a rapid change in anisotropic structure across the boundary itself (Wang and Wen, 2007; Cottaar and Romanowicz, 2013; Lynner and Long, 2014), with strong anisotropy concentrated just outside the LLSVP boundary. Further work that uses waveform modeling techniques to delineate the LLSVP edge in our study region, as has been done for other parts of the African LLSVP (e.g., Wang and Wen, 2004; Sun and Miller, 2012), is essential to confirm that our dataset is indeed sampling the region just outside the structure's edge, as assumed in our modeling approach and interpretation.

## 4.2. Implications for mantle flow and LLSVP dynamics

So far we have only considered our measurements in terms of single-crystal elasticity. To place our results in a geodynamic context, it is necessary to understand the relationship between deformation and seismic anisotropy. There is significant uncertainty as to how ppv deforms, with little consensus on the dominant slip system (e.g., Walker et al., 2011; Wenk et al., 2011). Experiments on analog materials suggest that [100] is the likely dominant slip direction in ppv, although other directions cannot be ruled out (Nowacki et al., 2011). The [100] direction may be the favored Burgers vector in terms of unit cell dimensions (Yamazaki and Karato, 2007), while some seismic observations also suggest that the [100] direction may be favored (Nowacki et al., 2010). We therefore interpret our best-fitting ppv orientations in terms of dominant slip in the [100] direction, with the caveat that this is the most likely possibility among several, and further work on deformation mechanisms in ppv is needed.

Assuming the development of LPO through dislocation creep, the slip direction should be generally oriented parallel to macroscopic flow (Karato, 2008). The orientations of our computed [100] axes (Fig. 6) can therefore be used to evaluate potential mantle flow geometries. Conceptual models for the origin and evolution of LLSVPs (McNamara and Zhong, 2005; Torsvik et al., 2008; Dziewonski et al., 2010) suggest a few plausible scenarios. These include 1) horizontal flow oriented perpendicular to the LLSVP edge, driven by slab remnants that aggregate material into thermochemical piles, 2) horizontal flow deflected along the LLSVP edge, 3) flow deflected upwards by the LLSVP edge, in a (nearly) vertical orientation, or 4) upwelling associated with mantle plume generation at the CMB. Of these simple scenarios, those that invoke horizontal flow are the least compatible with our anisotropy observations. While there are a few [100] orientations with nearly horizontal inclinations permitted by the data (Fig. 6), these points appear to be outliers among the 27 total orientations; additionally,

three of these four possibilities rely on a less likely explanation for the ScS null measurements.

The remaining 23 plausible ppv models, grouped into 4 effectively similar orientations (Fig. 6), exhibit [100] axes that are either nearly vertical or are significantly inclined (∼40°) from the horizontal. We suggest, therefore, that lowermost mantle flow beneath the Afar region likely has a significant vertical component. While we cannot rule out downwelling, most conceptual models for LLSVP evolution would propose upwards flow as a more likely possibility. Our observations thus suggest one of two geodynamically plausible scenarios (Fig. 6). The first is that lowermost mantle flow is nearly vertical (Clusters #1 and #3 in Fig. 6) with a horizontal gradient in flow velocity, resulting in finite strain orientations that are oriented nearly vertically. This deformation geometry may be consistent with either the upward deflection of flow at the LLSVP edge or with a local sheet-like upwelling. The second is that finite strain is oriented at an angle of ∼40° from the horizontal and directed to the southwest or southeast (Clusters #2 and #4 in Fig. 6), likely associated with oblique flow with a significant vertical component. This may be consistent with a transition from horizontal to more vertical flow as mantle material approaches the LLSVP edge, perhaps driven by paleoslab remnants from the north (Steinberger and Torsvik, 2012).

We can also consider the geodynamic implications of the polycrystalline aggregate modeling described in Section 3.4. Fig. 7 demonstrates that there are several orientations using the candidate (001) and (010) slip planes that are consistent with a nearly vertical shear direction, as might result from mantle flow at the LLSVP edge with a strong vertical component and a horizontal gradient in flow velocity. However, there are also cases where the shear direction is closer to horizontal (Fig. 7), which means we cannot rule out more nearly horizontal flow for these elastic constants. In any case, the uncertainties associated with models of lowermost mantle anisotropy based on polycrystalline plasticity are large (Walker et al., 2011; Wenk et al., 2006, 2011). A consideration of these more complex textures yields scenarios that are consistent with our preferred models based on single-crystal elasticity, but further work comparing predictions based on global flow models and texture modeling with splitting observations will be crucial.

Our observations and modeling cannot uniquely constrain the anisotropy orientation or mantle flow direction; however, we can quantitatively evaluate a range of anisotropic geometries and discriminate among simple but geodynamically plausible flow models. We reiterate that we have made fairly restrictive assumptions regarding the homogeneity of anisotropic structure within our study region, and that alternative explanations that invoke small-scale heterogeneity of anisotropy cannot be ruled out. Within the framework of our modeling approach, our preferred mantle flow scenarios (Fig. 6) are consistent with previous suggestions that strong deformation is likely concentrated just outside the boundaries of the African LLSVP, while its interior may remain relatively undeformed (Wang and Wen, 2007; Cottaar and Romanowicz, 2013; Lynner and Long, 2014). The geographic link between the likely vertical mantle flow we infer and the surface expression of the putative Afar plume (Ebinger and Sleep, 1998) is suggestive, although not definitive. Recent geodynamical modeling of plume generation at LLSVP edges (Steinberger and Torsvik, 2012) suggests the formation of sheet-like upwellings in the lowermost mantle, consistent with our observations. Regardless of the exact geometry of flow, however, our findings suggest that LLSVPs influence the pattern of flow at the base of the mantle. Future work to explore the assumptions we have made in this study regarding the homogeneity of anisotropic structure, and to apply our modeling framework to other regions and compare the inferred anisotropic geometry to our findings here, will be essential.

## 5. Summary

We have investigated shear wave splitting due to anisotropy in the lowermost mantle beneath the Afar region of Africa, just outside the boundary of thee African LLSVP, for a group of raypaths that encompass a range of propagation directions. Forward modeling of our observations using candidate elastic tensors, mostly derived from single-crystal elasticity of lowermost mantle minerals, reveals that the observations are compatible with only a limited number of anisotropic scenarios. Importantly, our results indicate that models that invoke VTI are not sufficient to explain our observations. This represents a significant departure from many previous studies of anisotropy in the lowermost mantle, which often assume a transversely isotropic geometry. Our preferred model for anisotropy and deformation just outside the boundary of the LLSVP invokes the LPO of ppv, with a finite strain direction (assumed to align with the [100] axis of ppv) that deviates significantly from the horizontal. Of the plausible mantle flow scenarios that have been previously suggested in the literature, our observations are most compatible with flow being deflected in a vertical direction at the LLSVP edge or with the formation of a sheet-like upwelling. While we cannot entirely rule out other scenarios – such as those that invoke a contribution from multiple mineral phases, or small-scale variations in deformation geometry – our analysis suggests that vertical flow at the edge of the LLSVP is consistent with the observations.

A number of assumptions were made in our raypath selection, forward modeling scheme, and interpretation of our results in terms of mantle dynamics scenarios. We anticipate that many of these assumptions will be tested as knowledge of the single-crystal elastic constants, dominant slip systems, deformation geometries, and small-scale heterogeneity at the base of the mantle continues to improve. The full consideration of predictions of lowermost mantle anisotropy from a suite of global mantle flow models (Walker et al., 2011) and the investigation of possible finite-frequency effects on the splitting predictions (e.g., Zhao and Chevrot, 2011) are also ongoing. We suggest that the observational and modeling approach used in this paper, which involves the construction of body wave datasets that sample a region of D″ over a range of propagation directions and the quantitative modeling of splitting observations, represents a powerful tool for constraining the anisotropy and deformation of the lowermost mantle.

## Acknowledgements

## References

Burke, K., Steinberger, B., Torsvik, T.H., Smethurst, M.A., 2008. Plume Generation Zones at the margins of Large Low Shear Velocity Provinces on the core–mantle boundary. Earth Planet. Sci. Lett. 265, 49–60.

Cobden, L., Mosca, I., Trampert, J., Ritsema, J., 2012. On the likelihood of post-perovskite near the core–mantle boundary: a statistical interpretation of seismic observations. Phys. Earth Planet. Inter. 210, 21–35.

Cottaar, S., Romanowicz, B.A., 2013. Observations of changing anisotropy across the southern margin of the African LLSVP. Geophys. J. Int. 195, 1184–1195.

Cottaar, S., Li, M., McNamara, A.K., Romanowicz, B., Wenk, H.R., 2014. Synthetic seismic anisotropy models within a slab impinging on the core–mantle boundary. Geophys. J. Int. 199, 164–177.

Davies, D.R., Goes, S., Davies, J.H., Schuberth, B.S.A., Bunge, H.-P., Ritsema, J., 2012. Reconciling dynamic and seismic models of Earth's lower mantle: the dominant role of thermal heterogeneity. Earth Planet. Sci. Lett. 353, 253–269.

Dziewonski, A.M., Lekic, V., Romanowicz, B.A., 2010. Mantle Anchor Structure: an argument for bottom up tectonics. Earth Planet. Sci. Lett. 299, 69–79.

Ebinger, C.J., Sleep, N.H., 1998. Cenozoic magmatism throughout east Africa resulting from impact of a single plume. Nature 395, 788–791.

Garnero, E.J., 2000. Heterogeneity of the lowermost mantle. Annu. Rev. Earth Planet. Sci. 28, 509–537.

Grocholski, B., Catalli, K., Shim, S.-H., Prakapenka, V., 2012. Mineralogical effects on the detectability of the postperovskite boundary. Proc. Natl. Acad. Sci. 109, 2275–2279.

He, X., Long, M.D., 2011. Lowermost mantle anisotropy beneath the northwestern Pacific: evidence from PcS, ScS, SKS, and SKKS phases. Geochem. Geophys. Geosyst. 12, Q12012. http://dx.doi.org/10.1029/2011GC003779.

Karato, S., 1998. Some remarks on the origin of seismic anisotropy in the D″ layer. Earth Planets Space 50, 1019–1028.

Karato, S.-i., 2008. Deformation of Earth Materials: An Introduction to the Rheology of Solid Earth. Cambridge University Press, Cambridge, UK.

Karki, B., Wentzcovitch, R.M., De Gironcoli, S., Baroni, S., 1999. First-principles determination of elastic anisotropy and wave velocities of MgO at lower mantle conditions. Science 286, 1705–1707.

Kendall, J.M., Silver, P.G., 1996. Constraints from seismic anisotropy on the nature of the lowermost mantle. Nature 381, 409–412.

Kennett, B.L.N., Engdahl, E.R., Buland, R., 1995. Constraints on seismic velocities in the Earth from traveltimes. Geophys. J. Int. 122, 108–124.

Lay, T., Williams, Q., Garnero, E.J., 1998. The core–mantle boundary layer and deep Earth dynamics. Nature 392, 461–468.

Lekic, V., Cottaar, S., Dziewonski, A., Romanowicz, B., 2012. Cluster analysis of global lower mantle tomography: a new class of structure and implications for chemical heterogeneity. Earth Planet. Sci. Lett. 357, 68–77.

Lin, Y.-P., Zhao, L., Hung, S.-H., 2014. Full-wave effects on shear wave splitting. Geophys. Res. Lett. 41, 799–804. http://dx.doi.org/10.1002/2013GL058742.

Long, M.D., 2009. Complex anisotropy in D″ beneath the eastern Pacific from SKS–SKKS splitting discrepancies. Earth Planet. Sci. Lett. 283, 181–189.

Long, M.D., Silver, P.G., 2009. Shear wave splitting and mantle anisotropy: measurements, interpretations, and new directions. Surv. Geophys. 30, 407–461.

Lynner, C., Long, M.D., 2013. Sub-slab seismic anisotropy and mantle flow beneath the Caribbean and Scotia subduction zones: effects of slab morphology and kinematics. Earth Planet. Sci. Lett. 361, 367–378.

Lynner, C., Long, M.D., 2014. Lowermost mantle anisotropy and deformation along the boundary of the African LLSVP. Geophys. Res. Lett. 41, 3447–3454. http://dx.doi.org/10.1002/2014GL059875.

McNamara, A.K., Zhong, S., 2005. Thermochemical structures beneath Africa and the Pacific Ocean. Nature 437, 1136–1139.

Meade, C., Silver, P.G., Kaneshima, S., 1995. Laboratory and seismological observations of lower mantle isotropy. Geophys. Res. Lett. 22, 1293–1296.

Mitrovica, J.X., Forte, A.M., 2004. A new inference of mantle viscosity based upon joint inversion of convection and glacial isostatic adjustment data. Earth Planet. Sci. Lett. 225, 177–189.

Montagner, J.P., Anderson, D.L., 1989. Petrological constraints on seismic anisotropy. Phys. Earth Planet. Inter. 54, 82–105.

Ni, S.D., Tan, E., Gurnis, M., Helmberger, D., 2002. Sharp sides to the African super-plume. Science 296, 1850–1852.

Niu, F., Perez, A.M., 2004. Seismic anisotropy in the lower mantle: a comparison of waveform splitting of SKS and SKKS. Geophys. Res. Lett. 31, L24612. http://dx.doi.org/10.1029/2004GL021196.

Nowacki, A., Wookey, J., Kendall, J.-M., 2010. Deformation of the lowermost mantle from seismic anisotropy. Nature 467, 1091–1094.

Nowacki, A., Wookey, J., Kendall, J., 2011. New advances in using seismic anisotropy, mineral physics and geodynamics to understand deformation in the lowermost mantle. J. Geodyn. 52, 205–228.

Nowacki, A., Walker, A.M., Wookey, J., Kendall, J.M., 2013. Evaluating post-perovskite as a cause of D″ anisotropy in regions of palaeosubduction. Geophys. J. Int. 192, 1085–1090.

Panning, M., Romanowicz, B.A., 2006. A three-dimensional radially anisotropic model of shear velocity in the whole mantle. Geophys. J. Int. 167, 361–379.

Simmons, N.A., Forte, A.M., Grand, S.P., 2009. Joint seismic, geodynamic and mineral physics constraints on three-dimensional mantle heterogeneity: implications for the relative importance of thermal versus compositional heterogeneity. Geophys. J. Int. 177, 1284–1304.

Simmons, N.A., Forte, A.M., Boschi, L., Grand, S.P., 2010. GyPSuM: a joint tomographic model of mantle density and seismic wave speeds. J. Geophys. Res. 115, B12310. http://dx.doi.org/10.1029/2010JB007631.

Stackhouse, S., Brodholt, J.P., Wookey, J., Kendall, J.-M., Price, G.D., 2005. The effect of temperature on the seismic anisotropy of the perovskite and post-perovskite polymorphs of MgSiO$_3$. Earth Planet. Sci. Lett. 230, 1–10.

Steinberger, B., Torsvik, T.H., 2012. A geodynamic model of plumes from the margins of Large Low Shear Velocity Provinces. Geochem. Geophys. Geosyst. 13, Q01W09. http://dx.doi.org/10.1029/2011GC003808.

Sun, D., Miller, M.S., 2012. Study of the western edge of the African Large Low Shear Velocity Province. Geochem. Geophys. Geosyst. 14, 3109–3125. http://dx.doi.org/10.1002/ggge.20185.

Torsvik, T.H., Steinberger, B., Cocks, L.R.M., Burke, K., 2008. Longitude: linking Earth's ancient surface to its deep interior. Earth Planet. Sci. Lett. 276, 273–282.

van der Hilst, R.D., de Hoop, M.V., Wang, P., Shim, S.-H., Tenorio, L., 2007. Seismostratigraphy and thermal structure of Earth's core–mantle boundary region. Science 315, 1813–1817.

Vidale, J.E., 1986. Complex polarization analysis of particle motion. Bull. Seismol. Soc. Am. 76, 1393–1405.

Walker, A.M., Forte, A.M., Wookey, J., Nowacki, A., Kendall, J.-M., 2011. Elastic anisotropy of $D''$ predicted from global models of mantle flow. Geochem. Geophys. Geosyst. 12, Q10006. http://dx.doi.org/10.1029/2011GC003732.

Walker, A.M., Wookey, J., 2012. MSAT—a new toolkit for the analysis of elastic and seismic anisotropy. Comput. Geosci. 49, 81–90.

Wang, Y., Wen, L., 2004. Mapping the geometry and geographic distribution of a very low velocity province at the base of the Earth's mantle. J. Geophys. Res. 109, B10305. http://dx.doi.org/10.1029/2003JB002674.

Wang, Y., Wen, L., 2007. Complex seismic anisotropy at the border of a very low velocity province at the base of the Earth's mantle. J. Geophys. Res. 112, B09305. http://dx.doi.org/10.1029/2006JB004719.

Wenk, H.-R., Cottaar, S., Tomé, C.N., McNamara, A., Romanowicz, B., 2011. Deformation in the lowermost mantle: from polycrystal plasticity to seismic anisotropy. Earth Planet. Sci. Lett. 306, 33–45.

Wenk, H.-R., Speziale, S., McNamara, A.K., Garnero, E.J., 2006. Modeling lower mantle anisotropy development in a subducting slab. Earth Planet. Sci. Lett. 245, 302–314.

Wentzcovitch, R.M., Tsuchiya, T., Tsuchiya, J., 2006. MgSiO$_3$ postperovskite at $D''$ conditions. Proc. Natl. Acad. Sci. USA 103, 543–546.

Wookey, J., Kendall, J., 2008. Constraints on lowermost mantle mineralogy and fabric beneath Siberia from seismic anisotropy. Earth Planet. Sci. Lett. 275, 32–42.

Wookey, J., Kendall, J., Rümpker, G., 2005a. Lowermost mantle anisotropy beneath the north Pacific from differential S–ScS splitting. Geophys. J. Int. 161, 829–838.

Wookey, J., Stackhouse, S., Kendall, J.M., Brodholt, J., Price, G.D., 2005b. Efficacy of the post-perovskite phase as an explanation for lowermost-mantle seismic properties. Nature 438, 1004–1007.

Wüstefeld, A., Bokelmann, G., Zaroli, C., Barruol, G., 2008. SplitLab: a shear-wave splitting environment in Matlab. Comput. Geosci. 34, 515–528.

Yamazaki, D., Karato, S.-i., 2007. Lattice-preferred orientation of lower mantle materials and seismic anisotropy in the $D''$ layer. In: Hirose, K., et al. (Eds.), Post-perovskite: The Last Mantle Phase Transition. In: American Geophysical Union Geophysical Monograph Series, vol. 174, pp. 69–78.

Zhao, L., Chevrot, S., 2011. An efficient and flexible approach to the calculation of three-dimensional full-wave Fréchet kernels for seismic tomography – II. Numerical results. Geophys. J. Int. 185, 939–954.